Renedo, J., Cuerno, R., Castro, M. y Muñoz García J. (2016). Symmetry of surface nanopatterns induced by ion-beam sputtering: Role of anisotropic surface diffusion. *Physical Review B*, 93 (15), 155424.

DOI: 10.1103/PhysRevB.93.155424

Symmetry of surface nanopatterns induced by ion-beam sputtering: Role of anisotropic surface diffusion

Javier Renedo,[1] Rodolfo Cuerno,[2] Mario Castro,[3] and Javier Muñoz-García[2]
[1]*Instituto de Investigación Tecnológica (IIT), Universidad Pontificia Comillas, 28015 Madrid, Spain*
[2]*Departamento de Matemáticas and Grupo Interdisciplinar de Sistemas Complejos (GISC), Universidad Carlos III de Madrid, 28911 Leganés, Spain*
[3]*GISC and Grupo de Dinámica No Lineal (DNL), Escuela Técnica Superior de Ingeniería (ICAI), Universidad Pontificia Comillas, 28015 Madrid, Spain*
(Received 29 December 2015; revised manuscript received 29 March 2016; published 19 April 2016)

Ion-beam sputtering (IBS) is a cost-effective technique able to produce ordered nanopatterns on the surfaces of different materials. To date, most theoretical studies of this process have focused on systems which become amorphous under irradiation, e.g., semiconductors at room temperature. Thus, in spite of the large amount of experimental work on metals, or more recently on semiconductors at high temperatures, such experimental contexts have received relatively little theoretical attention. These systems are characterized by transport mechanisms, e.g., surface diffusion, which are anisotropic as a reflection of the crystalline structure not being overruled by the irradiation. Here, we generalize a previous continuum theory of IBS at normal incidence, in order to account for anisotropic surface diffusion. We explore systematically our generalized model in order to understand the role of anisotropy in the space-ordering properties of the resulting patterns. In particular, we derive a height equation which predicts morphological transitions among hexagonal and rectangular patterns as a function of system parameters and employ an angular correlation function to assess these pattern symmetries. By suitably choosing experimental conditions, it is found that one might be able to experimentally control the type of order displayed by the patterns produced.

DOI: 10.1103/PhysRevB.93.155424

I. INTRODUCTION

Ion-beam sputtering (IBS) is a technique employed to efficiently nanostructure surfaces [1]: a solid target is bombarded with energetic ions, which erode material inducing self-organized pattern formation at the target surface. There is a wide technological interest in this technique, since it allows us to obtain ordered nanostructures with controlled roughness, wavelength, and orientation [2,3]. Moreover, it is scalable, cost efficient, and can be used in many materials, including semiconductors, metals, and insulators. One challenge that still limits the widespread use of IBS is the lack of a unified theoretical framework which guides experimental designs.

In this regard, continuum models have been relatively successful in describing the dynamical behavior of these nanostructures, typically in terms of macroscopic variables like the target surface height. For materials which are or become amorphous under low-energy ($E \simeq 1$ keV) IBS, such as semiconductors [4], Bradley and Harper (BH) pioneered this approach through a linear continuum theory which explains the formation of ripples and their orientation [5], based on Sigmund's theory of sputtering [6] and Mullins' thermal surface diffusion [7]. The success of this model in accounting for the origin of the patterns triggered an intense activity and further generalizations. In particular, relevant nonlinear corrections were identified in Ref. [8], leading to an equation of the Kuramoto-Sivashinsky (KS) type [9]. Importantly, nonlinearities were seen to moderate the pattern-forming linear instability and eventually stabilize the surface morphology.

The BH equation and its generalizations were similarly derived as in Ref. [5], by adding together physically diverse contributions into a single equation for the target height. Alternatively, as shown in Refs. [10] and [11], one can describe the dynamics of two different fields, the surface height and the density of material (e.g., adatoms, advacancies) subject to transport at the surface. This approach describes surface dynamics successfully in many different contexts, from granular matter [12] to epitaxial growth [13]. In the IBS context, it enables improvements [9], most notably by coupling different physical mechanisms in a natural way. For instance irradiation is expected to influence surface diffusion and be reflected in the corresponding terms in the height equation, typically as a linear high-order derivative term. However, direct expansion of Sigmund's contribution in the erosion velocity to such linear [14,15] or nonlinear orders [16,17] are affected by consistency issues with respect to pattern formation [18–20]. Such types of issues do not occur in two-field formulations [9]. Thus, the KS equation was consistently generalized into the so-called extended KS (eKS) model for IBS [21,22]. For normal incidence conditions, this model has been studied for one-dimensional (1D) systems [23], and for 2D systems and rotating targets [24]. Oblique incidence is studied in Ref. [25]. While being a phenomenological approximation of fuller hydrodynamic descriptions [26], two-field modeling provides a generic framework which allows us to modify the interface equation when improved models of erosion and/or transport are considered. To date, the two-field model and/or the eKS equation have been (semi)quantitatively validated in several IBS experiments [27–31].

The scenario just described focuses almost exclusively on targets for which the crystalline structure is overruled by the IBS process. However, there are important instances in which this is not the case, most notably metals [2,32] and semiconductors at high temperature [33–35]. In both cases, the strong dependence of the diffusivities of adatoms and advacancies

on the crystallographic direction can play a crucial role in the pattern formation process. For metals, the surface is not amorphized after ion impact. For semiconductors, increasing temperatures above the recrystallization value analogously restores dynamical dominance of crystalline anisotropies. As discussed in Refs. [32] and [36] for metallic systems, two regimes can be distinguished: (i) *diffusive regime*, when pattern formation is governed by thermal surface diffusion, typically for intermediate temperatures and relatively low ion fluxes, and (ii) *erosive regime*, when pattern formation is controlled by the direction of the ion beam, usually for very high or very low temperatures and for large enough ion fluxes. For instance, the diffusive regime allows for anisotropic ripple formation under isotropic, normal incidence conditions, and in general implies that both the ripple wavelength and orientation are controlled by temperature [32]. This behavior cannot be explained using previous models of IBS for amorphous targets, in which the diffusive terms are isotropic. A generalization of the linear BH model to anisotropic materials was proposed in Refs. [37] and [38]. Some properties observed in IBS of metals could thus be described, but in this formulation surface transport does not couple with erosion in a natural way. Likewise, with a focus on strongly kinetic effects, previous two-field [10,11] and one-field models [33–35] have described crystalline anisotropies, but only at nonlinear order. However, in principle under these conditions surface diffusion currents need to include anisotropic linear terms [39,40], which account for, e.g., the direction dependence of barriers to adatom/advacancy diffusion on terraces, along step edges, etc. [41].

In view of the above, there is a need for studies in which crystalline anisotropies to material transport are systematically addressed, for surfaces undergoing low-energy IBS. Already the simplest scenario of anisotropic linear surface diffusion can lead to nontrivial modifications of pattern properties, even if possibly not modifying others, such as stability phase diagrams [39,40]. For instance, recent experiments with gold targets [30,42] have obtained highly ordered nanodot patterns by sequential ion-beam sputtering (SIBS). The procedure consisted of sputtering under normal incidence a prepatterned ripple structure previously obtained by oblique bombardment. When the initial surface is flat and not prepatterned, a more disordered dot pattern is obtained, which still shows square in-plane order [42]. Although the (isotropic) eKS model reproduces many of the experimental properties of the ensuing nanobead pattern [30,42], it is not able to predict this square symmetry, being limited to describing more isotropic, hexagonal order. Square patterns of dots have been also reported for IBS of semiconductor substrates such as Si or Ge, when metallic contaminants are co-deposited [43,44]. Even though contamination had been neglected in the original derivation of the eKS model, the latter has proven to have a large predictive power even for IBS experiments on Si where metallic impurities are known to be relevant [28]. Hence, it is conceivable that generalizations of the eKS equation that incorporate surface anisotropies can account for nonhexagonal (e.g., square) pattern symmetries.

In this paper we put forward a two-field model of IBS nanopatterning under conditions in which anisotropies to surface transport are relevant. As a basis for further studies, our goal is to demonstrate nontrivial effects arising already within the simplest anisotropic scenarios, which will motivate our choices in the modeling of both transport and irradiation-related mechanisms. As a result, we obtain a generalization of the eKS equation, which is integrated numerically for normal ion incidence. Our results show that anisotropic surface diffusion has nontrivial effects and allows us to reproduce nanopatterns with different local ordering structures in monoelemental systems, from hexagonal to square, akin to those experimentally reported for IBS of metals [30,42].

This paper is organized as follows. Our generalized two-field model with anisotropic diffusion is put forward in Sec. II. In principle, the model holds for arbitrarily oblique ion incidence. However, in order to isolate the effect of anisotropy in diffusion, rather than in irradiation, we then restrict ourselves to normal incidence. For this case we derive an equivalent interface equation which generalizes the eKS model. This nonlinear equation is studied numerically in Sec. III, where the effect of each one of the parameters which control the system behavior is discussed in detail. Finally, Sec. IV contains our conclusions and an outlook on future developments. Some details on our modeling are provided in the Appendix.

II. GENERALIZED TWO-FIELD MODEL

A. Derivation

A two-field model is a system of two coupled partial differential equations describing the temporal evolution of two important macroscopic variables [9]. The first variable corresponds to the height of the bombarded surface, $h(\boldsymbol{x},t)$, at substrate position $\boldsymbol{x} = (x,y)$ and time t. The second one describes the thickness (which, for a fixed atomic volume, is proportional to the density) of the mobile surface adatoms layer, $R(\boldsymbol{x},t)$. For semiconductors at room temperature, irradiation creates an amorphous layer with a thickness of the order of the ion range [4], within which transport can be described in terms of viscous flow [26,45,46]. However, for metals or for semiconductors at high temperatures, such amorphization does not take place [32,36], so that the surface layer on which transport occurs can be assumed to have roughly an atomic thickness. In such cases, the dynamics of h and R are coupled by mass conservation as

$$\frac{\partial R}{\partial t} = (1-\phi)\Gamma_{\mathrm{ex}} - \Gamma_{\mathrm{ad}} - \nabla\cdot\boldsymbol{J}, \tag{1}$$

$$\frac{\partial h}{\partial t} = -\Gamma_{\mathrm{ex}} + \Gamma_{\mathrm{ad}}. \tag{2}$$

Here, Γ_{ex} is a function that describes the rate at which target atoms are excavated (locally decreasing h) and can become mobile (locally increasing R), while Γ_{ad} models the rate of atom addition back to the solid (increasing h and decreasing R). The parameter $\phi \in [0,1]$ measures the fraction of eroded atoms that are actually sputtered away from the surface, while $\bar{\phi} = 1-\phi$ measures the fraction of eroded atoms that remain subject to transport at the surface.

Equation (1) includes an additional conserved current, $\boldsymbol{J}$, which accounts for surface transport mechanisms. For

instance, this current could readily incorporate Carter-Vishnyakov (CV) contributions [47] due to mass redistribution, believed to be relevant in the case of semiconductors at room temperature [48]. These have been employed in a number of similar two-field models for IBS of compound systems, or for IBS of monoelemental targets under concurrent impurity co-deposition; see, e.g., Ref. [49] for a partial overview. For monoelemental targets, CV-type effects can also be reflected in $\Gamma_{\rm ex}$ [21]. In any case, for metals or semiconductors at high temperatures this type of mass redistribution is not expected to play a role, nor is, on a more mesoscopic level, surface-confined viscous flow [26,45,46,50]. The main transport mechanism is expected to be, rather, thermal surface diffusion. Microscopically, this is an activated process for which energetic barriers exist, whose depths depend on the crystallographic directions [51]. On a more coarse-grained level, as, e.g., in Mullins' classic theory [7], surface diffusion is mediated by surface tension, which for metals is paradigmatically anisotropic [52]. Mathematically, we thus consider Fickian diffusion at the surface as described by

$$\boldsymbol{J} = -\boldsymbol{D}\nabla R, \tag{3}$$

where $\boldsymbol{D} \in \mathbb{R}^{2\times 2}$ is a (positive definite) diffusion tensor, rather than a constant, that implements the present type of anisotropy. Its most general form reads

$$\boldsymbol{D} = \boldsymbol{M}(\psi)\begin{bmatrix} D_{\parallel} & 0 \\ 0 & D_{\perp} \end{bmatrix}\boldsymbol{M}^{-1}(\psi) = \begin{bmatrix} D_{xx} & D_{xy} \\ D_{xy} & D_{yy} \end{bmatrix}, \tag{4}$$

where $\boldsymbol{M}(\psi)$ is a counterclockwise rotation matrix of angle ψ which gives the orientation of the fast diffusion direction with respect to the $\hat{\boldsymbol{x}}$ direction, so that $D_{\parallel} \geqslant D_{\perp} > 0$ without loss of generality. Accurate estimations of anisotropy in surface diffusion coefficients are in general complex, as many underlying atomistic processes (such as terrace diffusion, edge diffusion, or sticking to islands) are anisotropic. STM-based estimates for, e.g., Si(001) obtain that diffusion can be up to 1000 times faster along than across dimer rows [53]. For Au (111) faces, molecular dynamics simulations suggest a relative variation of the surface diffusion coefficient by up to 100 when considering different steps [54]. Still, many uncertainties exist; see, e.g., Ref. [51] for a review on the complexities of quantifying surface diffusion at surfaces. At any rate, we presently wish to explore (some of) the generic consequences that diffusion anisotropies may have when in competition with the kinetic processes induced by ion-beam irradiation.

Models of anisotropic surface diffusion which are similar to Eqs. (3) and (4) have been employed to describe the dynamics of, e.g., vicinal [55] and singular [56] surfaces in epitaxy, which have been experimentally validated [57]. Note that the present (surface diffusion) anisotropy is independent of that induced by ion bombardment under an oblique angle of incidence; consequently, it is still relevant under otherwise isotropic normal incidence conditions. In principle, $\boldsymbol{J}$ could incorporate additional terms, most notably (linear and nonlinear) contributions depending on the surface height, which are related with Ehrlich-Schwoebel (ES) anisotropic barriers to surface diffusion [33–35,41,58]. However, the morphological instability associated with these terms differs physically from the BH instability. In order to assess more clearly the interplay between anisotropic surface diffusion and IBS, at this stage ES-related mechanisms are left for further work. They are expected to play a significant role in patterns whose in-plane order extends to a longer range, and in which wavelength coarsening is more sizable, than in, e.g., experiments on nanobead formation [30,42].

In order to close the system of Eqs. (1) and (2), the excavation and addition rates have to be related to the density of adatoms (R) and to the geometry of the substrate (h and its space derivatives) themselves. For an arbitrary incidence angle θ and assuming that the projection of the ion beam is along the $\hat{\boldsymbol{x}}$ direction, we consider [21,22]

$$\Gamma_{\rm ex} = \alpha_0\left[1 + \alpha_{1x}\frac{\partial h}{\partial x} + \alpha_{2x}\frac{\partial^2 h}{\partial x^2} + \alpha_{2y}\frac{\partial^2 h}{\partial y^2} + \alpha_{3x}\left(\frac{\partial h}{\partial x}\right)^2 + \alpha_{3y}\left(\frac{\partial h}{\partial y}\right)^2\right], \tag{5}$$

where $\alpha_0 = \Phi Y_0/n_v > 0$ defines the excavation rate of a flat surface, being directly related to the sputtering yield, Y_0, the ion flux, Φ, and the number of atoms per unit volume in the solid, n_v. Typical values of these parameters in the class of experiments that we are describing imply [25] $\alpha_0 \approx 10^{-3}$ to 10^2 nm s^{-1}.

In Eq. (5) the terms with coefficients α_{1x}, α_{2j} correspond to the lowest linear-order approximation to the dependence of the sputtering yield on the local height derivatives, as in BH's theory [5], while those with coefficients α_{3j} characterize the corresponding lowest-order nonlinear corrections [8]. Explicit forms for these parameters can be derived from physical models of the influence of ion irradiation on the surface dynamics. Thus, assuming, e.g., the predominance of sputtering events as described within Sigmund's linear cascade approximation, the coefficients α_{ij} are shown to depend on physical parameters such as the average ion flux and energy, their penetration depth, and the lateral stragglings of the space distribution of collision cascades [8,15]. More recently, so-called crater function mechanisms [59,60] have additionally related the coefficients α_{ij} with material redistribution taking place at the surface.

Due to the assumed geometry for ion bombardment, for normal incidence ($\theta = 0$) one has $\alpha_{1x} = 0$, while $\alpha_{2x} = \alpha_{2y}$, $\alpha_{3x} = \alpha_{3y}$, as can be verified in the physical models just mentioned that provide specific dependencies of α_{ij} on physical parameters, in particular with the incidence angle. In general, in the absence of CV-type effects, one expects $\alpha_{2j} > 0$ leading to pattern formation (BH instability), while nonzero α_{3j} guarantee nonexponential increase of the surface roughness for long times, as mentioned above.

Finally, for the local addition rate we consider [22]

$$\Gamma_{\rm ad} = \gamma_0\left[R\left(1 + \gamma_{2x}\frac{\partial^2 h}{\partial x^2} + \gamma_{2y}\frac{\partial^2 h}{\partial y^2}\right) - R_{\rm eq}\right], \tag{6}$$

where $\gamma_0 > 0$ is the nucleation rate; i.e., $1/\gamma_0$ represents the average time in which adatoms incorporate to a flat surface, typically in the range of picoseconds. As discussed earlier [24,25], in the absence of ion-beam driving Eq. (6) describes Mullins' thermal surface diffusion, in such a way that $R_{\rm eq}$ is related with the surface concentration of mobile species, while $\gamma_{2j} \geqslant 0$ are surface tension coefficients which, in general, can also be anisotropic.

The two-field model (1)–(6) supports a flat solution in which the surface height erodes with a uniform speed and both h and R are space-independent functions [61]. Performing a standard linear stability analysis of perturbations of this solution which are periodic with wave vector $\boldsymbol{k}$, we can obtain the pattern wavelength, ℓ_i, along each direction $i = x, y$ within linear approximation. Specifically, we define $\ell_i = 2\pi/k_i^{\ell}$ as the length scales at which the dispersion relation is maximized in each direction. In our case [61], $k_i^{\ell} = (\epsilon\phi\gamma_0\alpha_{2i}/2D_i\gamma_{2i})^{1/2}$, where the nondimensional parameter $\epsilon \equiv \alpha_0/(\gamma_0 R_{\rm eq})$ turns out to be small as a consequence of the difference between the typical time scales associated with diffusion and the ion-beam driving [25]. Indeed, for the typical values of α_0 and γ_0 quoted above, and if $R_{\rm eq} \approx 1$ nm, then $\epsilon \approx 10^{-12}$ to 10^{-7}. This separation in time scales allows one to simplify the analysis of the mathematical model [Eqs. (1) and (2)] since it allows one to perform a multiple-scale perturbative analysis to obtain a closed equation for the height. Analysis that closely follows Ref. [25] (see the Appendix for full details) leads to an effective nonlinear equation for the time evolution of h, which reads

$$\begin{aligned}\frac{\partial h}{\partial t} &= \gamma_x \frac{\partial h}{\partial x} + \sum_{i=x,y} \Omega_{ij} \frac{\partial^2}{\partial i \partial j}\left(\frac{\partial h}{\partial x}\right) \\ &+ \sum_{i=x,y}\left[-\nu_i \frac{\partial^2 h}{\partial i^2} + \lambda_i^{(1)}\left(\frac{\partial h}{\partial i}\right)^2\right] \\ &- \sum_{i,j,k=x,y}\left[\mathcal{K}_{ijk}\frac{\partial^2}{\partial i\partial j}\left(\frac{\partial^2 h}{\partial k^2}\right) + \lambda_{ij}^{(2)}\frac{\partial^2}{\partial i\partial j}\left(\frac{\partial h}{\partial k}\right)^2\right],\end{aligned} \tag{7}$$

where the coefficients γ_x, Ω_{ij}, ν_i, $\lambda_i^{(j)}$, and $\mathcal{K}_{ijk}$ depend on ion energy, flux, incidence angle, etc., through their dependencies on α_{ij} and all other parameters entering $\Gamma_{\rm ex}$ and $\Gamma_{\rm ad}$, as specified in the Appendix in Eq. (A28).

Equation (7) is partially similar to the evolution equation obtained in Ref. [22] for isotropic surface diffusion and oblique ion incidence. However, in that case the only geometrical condition responsible for breaking the $x \leftrightarrow y$ symmetry was the nonzero value of the incidence angle, in such a way that the system was symmetric under space reflection in the y direction, but not in the x direction. In the case of Eq. (7), this same cause for space anisotropy is enhanced by anisotropic surface diffusion and by anisotropic surface tension. As a consequence, not only are the $x \leftrightarrow y$ and $x \leftrightarrow -x$ symmetries broken, but the $y \leftrightarrow -y$ symmetry is broken as well, now by the two latter conditions. The differences between Eq. (7) and the one obtained in Ref. [22] will be further discussed in the following sections, for the case of normal ion incidence.

B. Effective equation for normal incidence

Having as reference experimental behaviors those reported in Refs. [42] and [30], in which an initial Au-prepatterned surface was further irradiated at normal incidence, we will focus here on such condition $\theta = 0$. This implies [24,25] $\alpha_{1x} = 0$, $\alpha_{2x} = \alpha_{2y} = \alpha_2$, and $\alpha_{3x} = \alpha_{3y} = \alpha_3$, and will allow us to isolate the effects purely due to anisotropies in surface diffusion. For this reason, we will moreover assume isotropic surface tension, namely, $\gamma_{2x} = \gamma_{2y} = \gamma_2$. As in Refs. [42] and [30], we will also take x and y to be aligned with the substrate directions along which surface diffusivities are optimized. Under these conditions, both the excavation and the addition rates become isotropic, Eq. (7) taking the simpler form

$$\begin{aligned}\frac{\partial h}{\partial t} &= -\nu\nabla^2 h + \lambda^{(1)}(\nabla h)^2 \\ &- \nabla\cdot[\boldsymbol{\mathcal{K}}\nabla(\nabla^2 h)] - \nabla\cdot\{\boldsymbol{\Lambda_2}\nabla[(\nabla h)^2]\},\end{aligned} \tag{8}$$

where $\boldsymbol{\mathcal{K}}$ and $\boldsymbol{\Lambda_2}$ are matrices defined as

$$\boldsymbol{\mathcal{K}} = \begin{bmatrix}\mathcal{K}_x & 0\\ 0 & \mathcal{K}_y\end{bmatrix} \quad \text{and} \quad \boldsymbol{\Lambda_2} = \begin{bmatrix}\lambda_x^{(2)} & 0\\ 0 & \lambda_y^{(2)}\end{bmatrix}. \tag{9}$$

The number of independent parameters in Eqs. (8) and (9) has reduced dramatically, the remaining ones being $\nu = \phi\alpha_0\alpha_2$, $\lambda^{(1)} = -\phi\alpha_0\alpha_3$, $\mathcal{K}_i = D_i R_{\rm eq}\gamma_2 + (\phi R_{\rm eq}\alpha_0\gamma_2 - \bar{\phi}D_i\alpha_0/\gamma_0)\alpha_2$, and $\lambda_i^{(2)} = (\phi R_{\rm eq}\alpha_0\gamma_2 - \bar{\phi}D_i\alpha_0/\gamma_0)\alpha_3$, where $i = x, y$. It is important to note that, in contrast to the equation obtained in Refs. [22,24], in which only terms of the form $\nabla^2 h$ and $(\nabla h)^2$ appear under normal ion incidence, in the case of Eq. (8) the second-order derivatives $\partial^2/\partial x^2$ and $\partial^2/\partial y^2$ are weighted by parameters that depend on the different diffusion coefficients.

Under experimental conditions leading to pattern formation, $\nu > 0$ in Eq. (8). With respect to the coefficients of the linear fourth-order derivative term in this equation, note that they contain contributions that couple different physical mechanisms in a natural way. Thus, the contribution proportional to surface diffusivity and surface tension is completely analogous to the form of Mullins' surface diffusion, although note that the coefficients may also include ion-induced contributions which are temperature-independent [25]. The remaining term in $\mathcal{K}_i$ couples erosion (being proportional to α_2) with transport (surface diffusivity) and surface tension, further implementing ion-induced diffusivity. We will consider conditions in which this fourth-order derivative term has a net smoothing effect, so that $\mathcal{K}_i > 0$. Finally, we consider the products $\lambda^{(1)}\lambda_j^{(2)}$ to also be positive. Mathematically, this condition is required for Eq. (8) to be free of so-called "cancellation modes," known to occur under appropriate conditions in related continuum models, such as the anisotropic KS [62] and eKS [18,22] equations.

We next rescale Eq. (8) in order to work in dimensionless units. This allows us to perform generic statements on the system behavior, while at the same time it also simplifies the discussion by minimizing the number of free parameters. Hence, we define

$$x = \left(\frac{\mathcal{K}}{\nu}\right)^{\frac{1}{2}} x', \quad y = \left(\frac{\mathcal{K}}{\nu}\right)^{\frac{1}{2}} y', \quad t = \frac{\mathcal{K}}{\nu^2}t', \quad h = \frac{\nu}{\lambda^{(1)}}h',$$

where $\mathcal{K} = (\mathcal{K}_x + \mathcal{K}_y)/2$. Dropping the primes, Eq. (8) now reads

$$\begin{aligned}\frac{\partial h}{\partial t} &= -\nabla^2 h + (\nabla h)^2 - 2\nabla\cdot[\boldsymbol{A}\nabla(\nabla^2 h)] \\ &- 2r_0\nabla\cdot\{\boldsymbol{B}\nabla[(\nabla h)^2]\},\end{aligned} \tag{10}$$

where the matrices $\boldsymbol{A}$ and $\boldsymbol{B}$ are

$$\boldsymbol{A} = \frac{\boldsymbol{\mathcal{K}}}{\mathcal{K}_x + \mathcal{K}_y} = \begin{bmatrix} \alpha_x & 0 \\ 0 & 1-\alpha_x \end{bmatrix},$$

$$\boldsymbol{B} = \frac{\boldsymbol{\Lambda_2}}{\lambda_x^{(2)} + \lambda_y^{(2)}} = \begin{bmatrix} \beta_x & 0 \\ 0 & 1-\beta_x \end{bmatrix},$$

with

$$\alpha_x = \frac{\mathcal{K}_x}{\mathcal{K}_x + \mathcal{K}_y}, \quad \beta_x = \frac{\lambda_x^{(2)}}{\lambda_x^{(2)} + \lambda_y^{(2)}},$$

$$r_0 = \frac{\nu}{\lambda^{(1)}} \left(\frac{\lambda_x^{(2)} + \lambda_y^{(2)}}{\mathcal{K}_x + \mathcal{K}_y} \right).$$

Given that three independent rescalings have been performed on Eq. (8), which depends on six independent parameters, the final Eq. (10) depends on three independent constants only, α_x, β_x, and r_0. Note that in all the physically relevant cases, $r_0 > 0$.

It is interesting to stress some of the features of Eq. (10): (i) As expected, the anisotropies are only caused by the different diffusivities D_x and D_y. This is reflected in the fact that the parameters α_x and β_x will generally take values different from $1/2$. Therefore, the weights for both directions in the last two terms of Eq. (10) will be different. When $\alpha_x = \beta_x = 1/2$ the isotropic diffusion equation for normal incidence proposed in Ref. [21] is recovered. (ii) The dimensionless parameter r_0 is the squared ratio of two length scales. One of these length scales is computed as the ratio between the parameters of the conserved Kardar-Parisi-Zhang (KPZ) [22] nonlinear terms appearing in the equation, $\lambda_i^{(2)}$, and that of the nonconserved KPZ nonlinearity that ensues, $\lambda^{(1)}$, namely, $[(\lambda_x^{(2)} + \lambda_y^{(2)})/\lambda^{(1)}]^{1/2}$. The second length scale is set by the parameters of the linear terms, as $[(\mathcal{K}_x + \mathcal{K}_y)/\nu]^{1/2}$. The parameter combination r_0 thus provides an estimate of the relative relevance of the various contributions that compete in the dynamics of the system.

As just stressed, in general Eq. (10) is anisotropic; thus the patterns will present different wavelengths along each principal direction. These can be estimated as functions of the parameters of the equation, by performing a standard linear stability analysis [25]. This leads to

$$\ell_i = \frac{2\pi}{k_i^{\ell}} = 2\pi \sqrt{\frac{2\mathcal{K}_i}{\nu}} \approx 2\pi \sqrt{\frac{2D_i\gamma_{2i}}{\epsilon\phi\gamma_0\alpha_{2i}}}, \qquad (11)$$

where we have substituted the values of $\mathcal{K}_i$ and ν provided after Eq. (9). As expected, these wavelengths coincide with the values obtained in Sec. II for the linear stability analysis of the full two-field model. Importantly, the expressions obtained for ℓ_i can be often used to perform (semi)quantitative comparisons between the present type of continuum models and experiments at short times, prior to the onset of nonlinear effects [28,30,63].

III. RESULTS

Thus far, we have been able to derive an effective dimensionless equation for normal ion incidence that contains all the physical mechanisms of the problem and depends on three free parameters only, Eq. (10). In this section we study systematically this equation by independently changing the values of each of these three parameters. Given the strong nonlinearities in the equation, we resort to a numerical integration. Specifically, our code was implemented in MATLAB, being based on a standard finite-difference scheme in space (for the linear terms) and a fourth-order Runge-Kutta method for the time evolution, using a spatial grid with 256×256 nodes, a time step $\Delta t = 0.01$, and a space step $\Delta x = 1$. The discretization of the nonlinear terms was based on the one proposed by Lam and Shin in Ref. [64]. We have employed periodic boundary conditions and initial height values which are uniformly distributed between 0 and 0.1. Besides inspection of the resulting surface morphologies, in all cases we have calculated the global surface roughness, W, as well as the wavelengths, ℓ_x and ℓ_y, after averaging over 10 realizations of the initial condition for each parameter set. Additionally, we have computed the normalized autocorrelation function, R_N, that allows one to determine the local arrangement of the patterns and is defined as [65]

$$R_N(\boldsymbol{x},t) = \frac{1}{W}\frac{1}{L^2}\int [h(\boldsymbol{x}+\boldsymbol{r},t)h(\boldsymbol{r},t) - \bar{h}^2(t)]d\boldsymbol{r}, \qquad (12)$$

where W is the surface roughness and $\bar{h}$ is the mean height over the whole spatial grid of size $L\times L$.

A. Isotropic case: $\alpha_x = \beta_x = 1/2$

To begin with our analysis, and for the sake of later comparison with anisotropic parameter conditions, we first recall the results obtained in Ref. [24] for isotropic systems under normal ion incidence, as a special case of our model in which both surface diffusivities are equal, $D = D_x = D_y$. In this case Eq. (8) simply reduces to the eKS equation,

$$\frac{\partial h}{\partial t} = -\nu\nabla^2 h - \mathcal{K}\nabla^4 h + \lambda^{(1)}(\nabla h)^2 - \lambda^{(2)}\nabla^2(\nabla h)^2, \qquad (13)$$

where $\mathcal{K} = \mathcal{K}_x = \mathcal{K}_y$ and $\lambda^{(2)} = \lambda_x^{(2)} = \lambda_y^{(2)}$. After a rescaling which is similar to the one employed in the previous section, this equation reduces to the particular case of Eq. (10) in which $\alpha_x = \beta_x = 1/2$. Note that, in principle, the simulations reported in Ref. [24] correspond to the unrescaled Eq. (13).

The following features for the surface roughness and pattern wavelength were obtained in this case [24]: (i) The surface morphology shows a short-time transient behavior. During this interval W grows exponentially with time and a dot pattern appears whose characteristic wavelength is accurately described by the linear analysis. Indeed, this stage is controlled by the linear terms $\nu\nabla^2 h$ and $\mathcal{K}\nabla^4 h$. (ii) After this linear regime, a crossover takes place towards a behavior which is controlled by the conserved nonlinear term $\lambda^{(2)}\nabla^2(\nabla h)^2$, in which the growth of W and ℓ in time can be approximated by power laws, with effective exponents whose values depend on equation parameters. (iii) For long times, the nonconserved nonlinear term $\lambda^{(1)}(\nabla h)^2$ induces eventual saturation of W and ℓ, and height disorder at large scales.

Actually, the relative duration of the various dynamical regimes turns out to be controlled by the parameter r_0 [23,24]. Thus, large r_0 values correspond to the predominance of the conserved KPZ nonlinearity at intermediate times, allowing

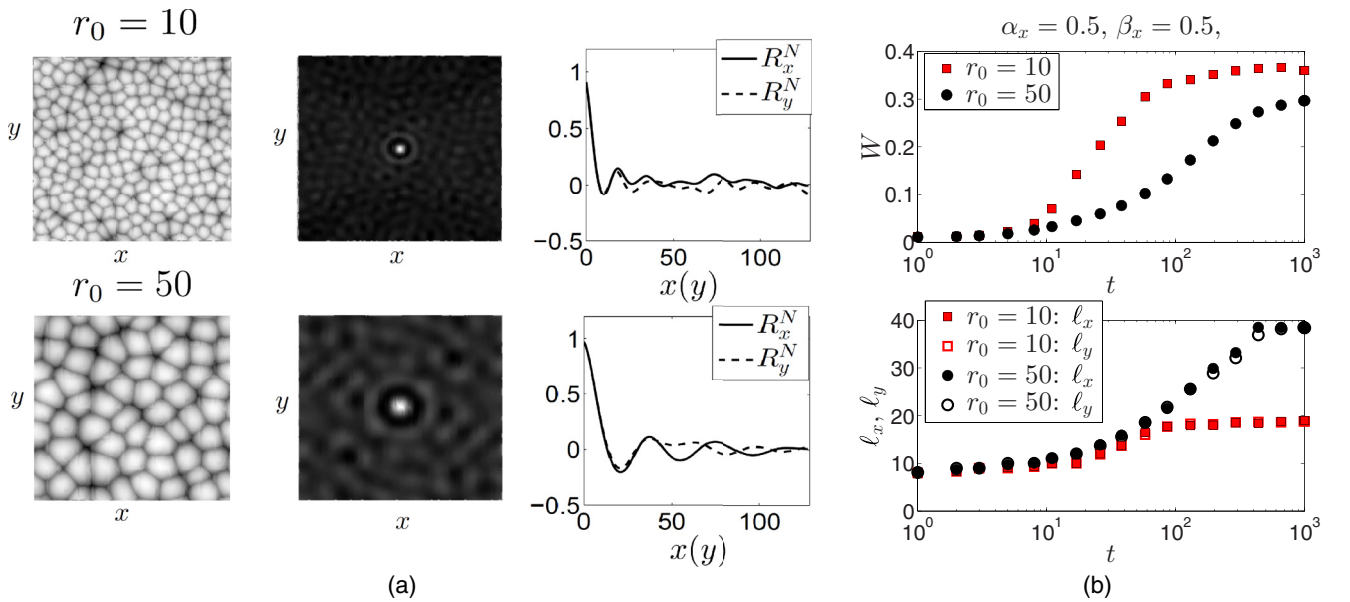

FIG. 1. (a) Top-view surface morphologies (left column), normalized autocorrelation functions, R_N (center column), and normalized autocorrelation functions along the x and y directions, R_x^N and R_y^N, respectively (right column), predicted by Eq. (10) at $t = 1000$ for $\alpha_x = 0.5$, $\beta_x = 0.5$, and different values of r_0 (see legends). (b) Temporal evolution of the roughness, W, and the wavelengths along the x and y directions, ℓ_x (solid symbols) and ℓ_y (open symbols), respectively, for the same parameter values as in (a).

for a stronger coarsening process and an improved order of the height values throughout the surface, namely, a smaller roughness. On the contrary, small r_0 values correspond to a nonlinear regime dominated by the KPZ nonlinearity, with a relatively short intermediate coarsening regime and a rougher surface at long times.

At this point, it is important to remark that the 1D and 2D behaviors of Eq. (13) differ quite strongly with respect to the ordering properties. To begin with, note that, given the fact that the band of unstable modes extends down to $\mathbf{k} = \mathbf{0}$, combined with the occurrence of the nonconserved KPZ nonlinearity, order in the pattern can be short range at most [66]. This does not prevent the equation from providing a quantitatively accurate description of experimental patterns [28,63]. Then, while relative homogeneity in height values correlates positively with an enhanced "in-plane" order for Eq. (13) in 1D [23], this is not the case in 2D. Namely, for the 2D case, smaller r_0 values seem to feature improved in-plane short-range hexagonal ordering of the dot structure. Conversely, larger values of r_0, which allow for stronger coarsening (wider cells) and smaller overall roughness, correspond to surfaces with poorer in-plane ordering. For a thus-far unreported explicit comparison, see Fig. 1, in which the $r_0 = 10$ and 50 cases are explicitly illustrated. The results shown in Fig. 1 also show that in both cases the wavelengths along each direction, ℓ_x and ℓ_y, are equal, since the surface diffusion is isotropic.

The rich crossover behavior of Eq. (13) will be useful to better understand the morphologies described by Eq. (10) as a function of parameter values.

B. General values of α_x

To study the effect of nonisotropic values of the parameter α_x mediating the linear surface-diffusion terms in Eq. (10), we have integrated numerically Eq. (10) for $r_0 = 10$, $\beta_x = 0.5$, and values of $\alpha_x \in [0, \frac{1}{2}]$. Due to the symmetry of Eq. (10) with respect to reflections of α_x around the isotropic 1/2 value, the behavior for $\alpha_x \in [\frac{1}{2}, 1]$ can be easily obtained from our simulations by simply swapping the x and y axes.

Figure 2(a) shows the surface morphologies, the normalized autocorrelation function, and cross-cuts of the normalized autocorrelation function along the x and y axes, R_x^N and R_y^N, respectively, at $t = 1000$ and for different values of α_x. Note that, as discussed above, $\alpha_x = 0.5$ corresponds to the isotropic case already studied in Ref. [24]. As noticed by inspecting the left column of the figure, the surface morphology does not change qualitatively for different values of α_x. This *robustness* with respect to α_x is further evidenced in the middle and right panels of Fig. 2(a), in which R^N is shown side-by-side with R_x^N and R_y^N. The x and y wavelengths, ℓ_x and ℓ_y, can be obtained by measuring the distance from the origin to the first maximum of the autocorrelation function along the corresponding axis. For all the values of α_x considered, we obtain $\ell_x \simeq \ell_y$, the only significant difference being that, for $\alpha_x = 0.25$ and $\alpha_x = 0.3$, the first peak of the autocorrelation function along the y direction is higher than the first peak along the x direction, both peaks having the same heights for $\alpha_x = 0.5$. This implies that, for $\alpha_x \in (0,0.5)$, dots are more correlated along the y direction, although the differences are not substantial.

Figure 2(b) shows the time evolution of the global roughness W and wavelengths, ℓ_x (solid symbols) and ℓ_y (open symbols), for the same values of α_x as in Fig. 2(a). As for the isotropic eKS model, three time regimes can be distinguished: Initially the roughness grows exponentially, up to intermediate times when its growth rate slows down; eventually it reaches a similar time-independent value for all α_x. On the other hand, the behavior of the pattern wavelengths with α_x is different. Initially both ℓ_x and ℓ_y start growing slowly, with ℓ_y being larger than ℓ_x for $\alpha_x < 0.5$. This is due to the fact that the fourth-order linear terms controlled by the parameter α_x are

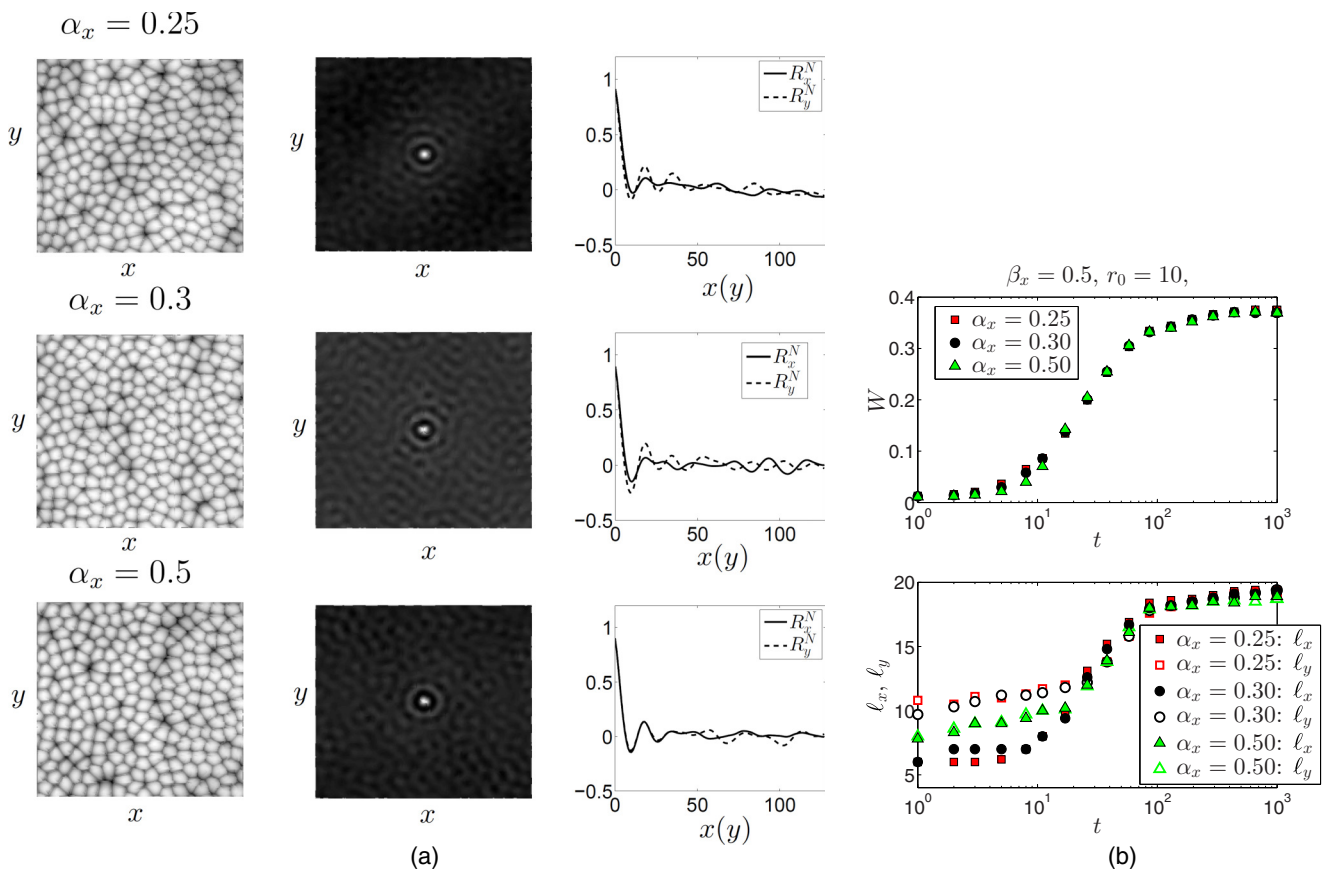

FIG. 2. (a) Top-view surface morphologies (left column), normalized autocorrelation functions, R_N (center column), and normalized autocorrelation functions along the x and y directions, R_x^N and R_y^N, respectively (right column), predicted by Eq. (10) at $t = 1000$ for $\beta_x = 0.5$, $r_0 = 10$, and different values of α_x (see legends). (b) Temporal evolution of the roughness, W, and the wavelengths along the x and y directions, ℓ_x (solid symbols) and ℓ_y (open symbols), respectively, for the same parameter values as in (a).

expected to play an important role precisely at the small spatial and time scales at which the linear instability develops. As a matter of fact, looking at the expressions of the wavelengths predicted by the linear instability analysis, Eq. (11), we can easily note that ℓ_x should be smaller than ℓ_y if $\mathcal{K}_x < \mathcal{K}_y$, which is indeed the case for $\alpha_x < 0.5$. This linear transient behavior is followed by a coarsening process controlled by the nonlinear terms, which finally drive both wavelengths to similar saturation values. Thus, since the parameters of the nonlinear terms r_0 and β_x are fixed, the final surface topographies are very similar at long times for the different values of α_x. Additionally, because the nonlinear terms are isotropic ($\beta_x = 0.5$) the wavelengths reach similar values in both directions at long times. In the next sections we study the impact of the coefficients of the nonlinear terms on the system dynamics and pattern formation and evolution.

C. General values of β_x

We next consider the influence on the topography of the anisotropic, conserved nonlinearity which is controlled in Eq. (10) by the parameter β_x. To this end, numerical integrations of Eq. (10) have been performed for fixed values of α_x and r_0, and $\beta_x \in [0, \frac{1}{2}]$. Similarly to the case of α_x, results for $\beta_x \in [\frac{1}{2}, 1]$ can be deduced from the simulations shown next by swapping the x and y axes. Figure 3(a) displays the morphology, the normalized autocorrelation function, and the autocorrelation function along the x and y axes at $t = 1000$ for different values of β_x. The additional case $\beta_x = 0.5$ for the chosen α_x corresponds to the isotropic system already shown on the third row of Fig. 2(a). The temporal evolution of the surface roughness and wavelengths is shown in Fig. 3(b).

If β_x is small, the conserved nonlinearity acts predominantly along the y axis, inducing stronger coarsening behavior, hence ℓ_y becomes larger than ℓ_x for times beyond the linear regime; see Fig. 3(b). Actually, this behavior is associated with a change in the pattern symmetry; see, e.g., the $\beta_x = 0.2$ case in Fig. 3(a). Indeed, the larger value of ℓ_y implies that the dots or cells become more elongated in the y direction, leading to the emergence of a ripple pattern with periodicity parallel to it or, equivalently, with ridges along the x axis. This can be noted both in the morphology and in the autocorrelation functions, and is in spite of the fact that we are considering normal incidence conditions for the ions. Note, this is a purely nonlinear effect, as Eq. (10) is completely isotropic *at linear order* for this parameter condition. On the other hand, if β_x increases, the elongation of the dots along the y direction is attenuated, they form arrangements with a more square (rather than rectangular) symmetry, and the effect is mitigated; see Fig. 3(a) for $\beta_x = 0.3$. At any rate, for $\beta_x \neq 1/2$ the isotropy of the pattern is clearly broken.

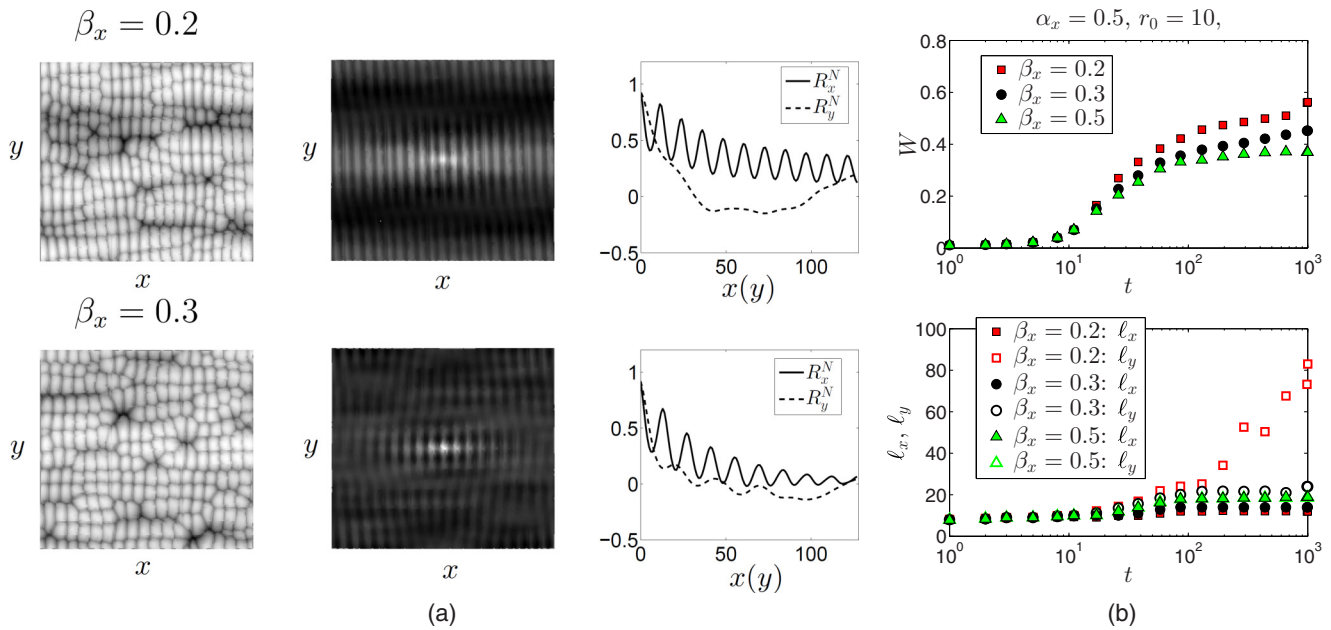

FIG. 3. (a) Top-view surface morphologies (left column), normalized autocorrelation functions, R_N (center column), and normalized autocorrelation functions along the x and y directions, R_x^N and R_y^N, respectively (right column), predicted by Eq. (10) at $t = 1000$ for $\alpha_x = 0.5$, $r_0 = 10$, and different values of β_x (see legends). (b) Temporal evolution of the roughness, W, and the wavelengths along the x and y directions, ℓ_x (solid symbols) and ℓ_y (open symbols), respectively, for the same parameter values as in (a).

With respect to the time evolution of the surface roughness, Fig. 3(b) indicates an unambiguous dependence with the value of β_x, which contrasts with the results obtained for α_x in the preceding section. For small values of β_x, saturation occurs later and the saturation value is larger. This seems reminiscent of results for the 1D eKS equation when increasing the strength of the conserved KPZ nonlinearity with respect to the remaining terms in the equation [23]. On the other hand, for short times the roughness values are practically the same for all β_x, suggesting that such an increase of the roughness is indeed a nonlinear effect. Regarding the pattern wavelengths in the two directions, both grow very slowly and take similar values during the short times associated with the linear instability. At intermediate times, both grow at increased rates; ultimately, they reach very different saturation values depending on the specific value of β_x. Indeed, as already noted above, for relatively small values of this parameter the pattern wavelength in the y direction, ℓ_y, becomes larger than ℓ_x, as can be clearly appreciated in Fig. 3(b) already for $\beta_x = 0.3$. For even smaller values of β_x, such as $\beta_x = 0.2$, ℓ_x interrupts its growth process early while ℓ_y keeps growing for a long time (note that its coarsening process has not yet stopped at $t = 1000$ for $\beta_x = 0.2$), resulting in very different $\ell_y > \ell_x$. This is due to the fact that the conserved nonlinear term, which induces the coarsening process, is stronger along the y direction. In summary, the role of β_x is twofold: it modifies the local arrangement (symmetry and order) of the patterns and it amplifies/reduces the coarsening dynamics selectively along one of the system directions.

D. General values of r_0

We continue in this section with the morphological effects of the third independent parameter in Eq. (10), namely, the ratio of nonlinear to linear length scales, r_0. The simulation results for different values of r_0 are shown in Fig. 4(a). Analogously to the isotropic case for normal incidence studied in Sec. III A and illustrated in Figs. 1(a) and 1(b), in the presence of anisotropic surface diffusion the patterns present more coarsening and a smaller roughness when r_0 is larger. However, the quality of in-plane ordering of the dots is poorer. For the parameter values considered in Fig. 4(a), slightly elongated dots group together following square arrangements, as can be noted looking at the surface morphologies. However, the short-range square order is hindered for larger r_0 values. This is also reflected in the autocorrelation function, where a more perfect square pattern is revealed for smaller values of r_0.

The temporal evolution of the roughness and wavelengths for different values of r_0 are represented in Fig. 4(b). Again three main regimes can be distinguished. The roughness grows exponentially in the first, linear regime, followed by power-law growth, and by saturation at very long times. As in Refs. [22] and [24], the final roughness is indeed smaller for large r_0 values, the long-time configurations showing more uniform height values. For such large r_0, the two wavelengths ℓ_x and ℓ_y are also larger, due to the longer coarsening process undergone. Note, because $\alpha_x = 0.5$, the linear terms have the same effect in both directions. Since $\beta_x = 0.3$ in the simulations shown, and as we saw in the previous section, the wavelength grows more in the y direction and patterns with $\ell_y > \ell_x$ are always obtained.

E. Unusual patterns and order under normal incidence: Ripples and square or hexagonal dot arrangements

As suggested by Fig. 4(a), for intermediate values of β_x it is possible to generate surfaces for which the dot patterns display short-range order with square symmetry. Such

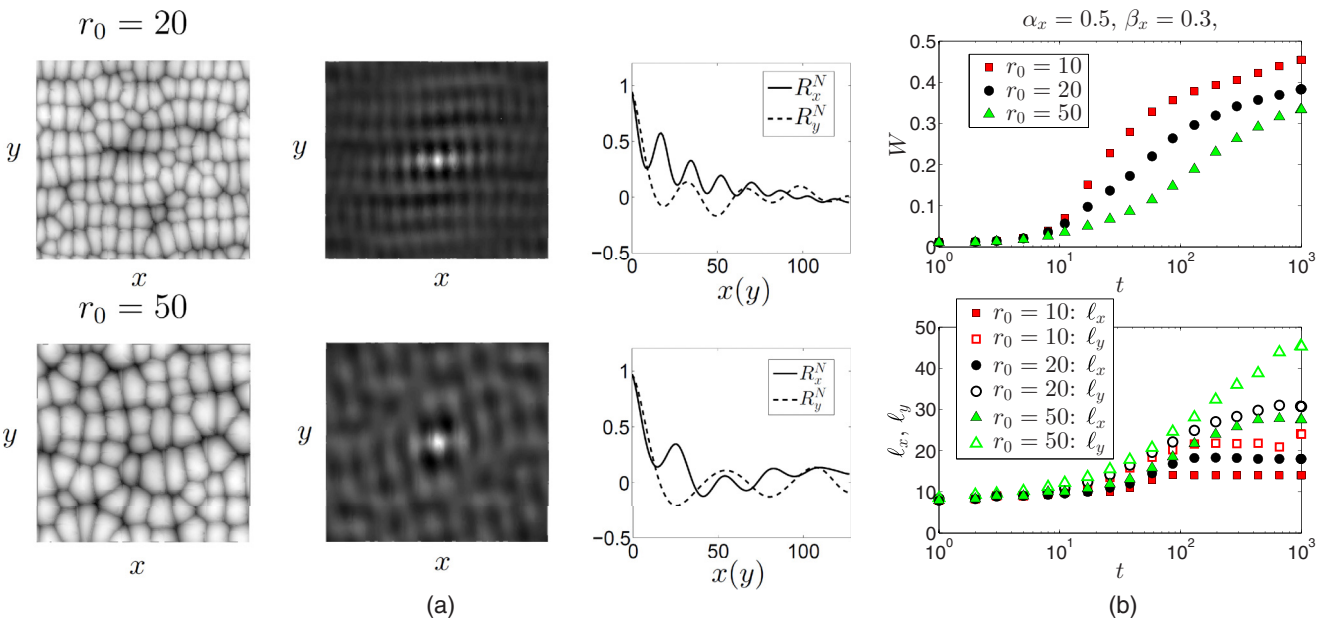

FIG. 4. (a) Top-view surface morphologies (left column), normalized autocorrelation functions, R_N (center column), and normalized autocorrelation functions along the x and y directions, R_x^N and R_y^N, respectively (right column), predicted by Eq. (10) at $t = 1000$ for $\alpha_x = 0.5$, $\beta_x = 0.3$, and different values of r_0 (see legends). (b) Temporal evolution of the roughness, W, and the wavelengths along the x and y directions, ℓ_x (solid symbols) and ℓ_y (open symbols), respectively, for the same parameter values as in (a).

a morphology is locally characterized by each single dot having on average four nearest neighbors located along the two Cartesian directions. Here we employ the normalized height autocorrelation function, R_N, to quantify the spatial order on the surface. If the morphology does correspond to a pattern with such a square-symmetric order, the central maximum of R_N lies within a perfect square formed by eight nearest satellite peaks on a square arrangement. Although the surfaces described by Eq. (10) present this type of structure to a certain degree, it is not possible to obtain a strictly square symmetry due to the anisotropy introduced by the conserved nonlinearities controlled by the parameter β_x. Indeed, the heterogeneous surface diffusivities in the two space directions lead to different wavelengths, even under isotropic (normal incidence) irradiation, producing a relatively ordered array of dots, but with different typical sizes in each direction. For $\beta \in (0,0.5)$, dots are more correlated with their neighbors along the x direction than along the y direction, as can be noticed in the height autocorrelation functions obtained in the previous sections. See for example Fig. 4(a), where the correlation values are clearly larger along the x axis. Recall that decreasing β_x in this range of values actually increases the elongation of dots along the y axis.

Enhancement of local square order can be achieved bringing together the previous property with the fact that local order is improved for relatively small r_0 values. Thus, Fig. 5 displays the surface morphologies obtained for $r_0 = 5$ and different values of β_x and their corresponding autocorrelation maps. The symmetry of the short-range order of the pattern can be identified easily in the autocorrelation map, which has been calculated for the (100×100) black boxes indicated. Indeed, since the morphology is disordered at long distances, some of the local order information is lost when the height autocorrelation function is computed in the whole domain. At any rate, Fig. 5 shows how dots with square-symmetric short-range order can actually occur for intermediate values of β_x when the elongation along the y direction exists but is not excessively pronounced.

Closer inspection of Fig. 5 actually suggests that up to three main types of patterns can be expected for Eq. (10), depending on the value of β_x: ripples (with a dotted substructure) and dots with square or with hexagonal short-range order. Moreover, as we have already seen, the degree of local order of the pattern can be enhanced by tuning the value of r_0. Indeed, the three main different patterns just mentioned can be clearly distinguished in Fig. 5, where $r_0 = 5$ has been fixed. In the case of isotropic surface diffusion ($\beta_x = 0.5$), dots with $\ell_x = \ell_y$ group into hexagonal short-range order, where each dot tends to be in the center of a hexagon formed by the nearest-neighbor dots, and local regions tend to have the same average height. For intermediate values $\beta_x \in [0.25, 0.3]$, square-ordered elongated dots with $\ell_y > \ell_x$ occur. Moreover, for these parameter values the surface heights becomes more heterogeneous, different local regions presenting different average heights. For even lower values of β_x, a ripple structure appears, with a periodicity along the y direction. Again this morphology displays quite heterogeneous average heights in different regions, while it still features a short-scale structure of rather elongated dots which are quite ordered along the x direction. Hence, decreasing the value of β_x induces a transition from short-range hexagonal, to square, and then to rectangular ordering of the dots.

An analogous transition between hexagonal and square patterns has been studied in Ref. [67] for the case of magnetic fluids under applied magnetic fields. In this work the authors employ an angular correlation function that makes use of the discrete Fourier transform of the height field in order to characterize the (hexagonal or square) symmetry of the pattern,

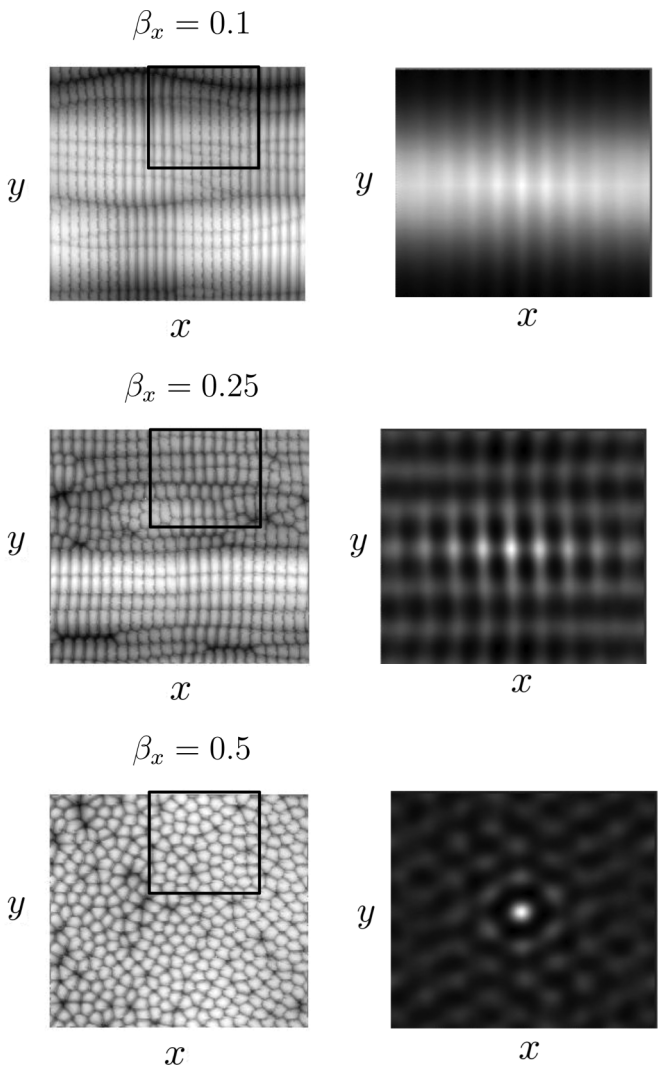

FIG. 5. Top-view surface morphologies (left column) predicted by Eq. (10) at $t = 1000$ for $\alpha_x = 0.5$, $r_0 = 5$, and different values of β_x (see legends). Corresponding normalized autocorrelation functions (right column) computed over the indicated squares of size 100×100.

and thus assess morphological transitions under changes in external parameters. Here, we define a similar angular correlation function, but relative to the values of R_N, rather than those of $h(\boldsymbol{x},t)$. Specifically, the angular autocorrelation function, $P(\psi,t)$, which we propose to quantify the pattern order is

$$P(\psi,t) = \frac{1}{L_w^2}\int \left[R_N(\boldsymbol{x},t)R_N(\boldsymbol{M}(\psi)\boldsymbol{x},t) - \bar{R}_N^2(t)\right]d\boldsymbol{x}, \quad (14)$$

where $\bar{R}_N(t)$ is the space average of the autocorrelation function, $R_N(\boldsymbol{x},t)$, over a square window of lateral size L_w, and as above $\boldsymbol{M}(\psi)$ is the counterclockwise rotation matrix of angle ψ. The function $P(\psi,t)$ thus measures the height correlation at every position in the considered domain and compares it with the result obtained at a position which is rotated by an angle ψ. We further define the normalized angular autocorrelation function as $P_N(\psi,t) = P(\psi,t)/P(0^\circ,t)$. The reason for considering an area of lateral size $L_w < L$ is because some rotated points $\boldsymbol{M}(\psi)\boldsymbol{x}$ could remain out of the considered domain for a square grid. Besides, due to the global disorder of the patterns induced by the KPZ nonlinearity, the short-range order of the pattern needs to be quantified in smaller areas.

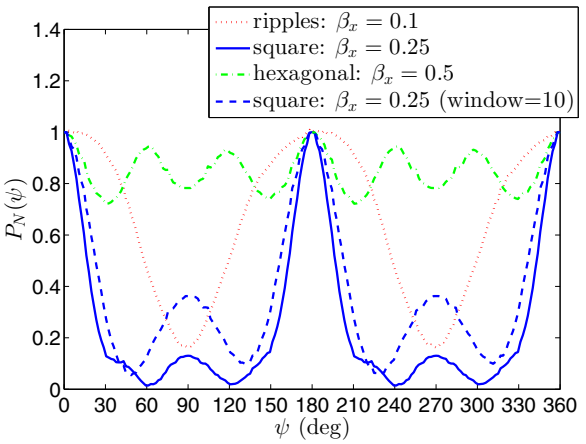

FIG. 6. Normalized angular autocorrelation function, $P_N(\psi,t)$, at $t = 1000$ with $L_w = 16$ for the morphologies in Fig. 5 in which $\beta_x = 0.1$ (dotted red line), $\beta_x = 0.25$ (solid blue line), and $\beta_x = 0.5$ (dash-dotted green line). The dashed blue line shows $P_N(\psi,t)$ for $\beta_x = 0.25$ with $L_w = 10$.

The normalized angular autocorrelation functions corresponding to the three basic morphologies shown in Fig. 5 are displayed in Fig. 6. The local extrema in $P(\psi,t)$ signal how well correlated are the points in the morphology with those rotated by an angle ψ. In all cases, due to the system symmetry under a 2D space inversion $(x,y) \to (-x,-y)$, this function is periodic with 180° period. For $\beta_x = 0.1$ (dotted red line) ripples form and the only rotation that leaves the system unchanged is precisely one with $\psi = 180^\circ$, hence the maxima in $P(\psi,t)$ as a function of ψ are separated by this value. A different behavior is found for $\beta_x = 0.25$ (solid blue line), when a dot pattern with square-symmetric order appears. In this case the distance between consecutive maxima of $P(\psi,t)$ is 90°, since the height correlation is itself maximized after a rotation of 90° for a pattern with this type of order. Note that, due to the large-scale disorder of the morphology, secondary maxima are smaller than 1, indicating a smaller degree of correlation. Improved correlation values for the secondary maxima are obtained for $\beta_x = 0.5$ (dash-dotted green line), when dots group into short-range hexagonal order. In this case the angular autocorrelation function suggests the best correlation among surface points for $\psi = 60^\circ$ and $\psi = 120^\circ$, signaling hexagonal symmetry in the dot arrangement.

We should remark that the size of the patterns and the spatial range of the order can be different in each parameter regime, which requires suitable window sizes for appropriate assessment. In particular, the square-order dots pattern reaches smaller distances than the ripples or the hexagonal dots pattern, so that the maxima of the corresponding angular autocorrelation function are smaller if the same lateral window size is employed. As an example, the angular autocorrelation function for $\beta_x = 0.25$ using a smaller window is shown by the dashed blue line in Fig. 6. We note that this window size is more appropriate to measure the square-order pattern, since

the peak values of the angular autocorrelation at $\psi = 90^\circ$ and $\psi = 270^\circ$ are larger and, therefore, the square pattern can be identified better.

IV. DISCUSSION AND CONCLUSIONS

Motivated by the experimental results in Refs. [42] and [30], we have generalized the eKS model proposed in Refs. [21] and [22] for anisotropic materials considering anisotropic surface diffusion. We have obtained a continuum equation for the surface height, Eq. (8), which, in contrast to the isotropic eKS model, presents anisotropies caused by the heterogeneous diffusivities along each substrate direction. This model allows to reproduce rippled and square-ordered patterns for normal incidence, akin to those observed in IBS of metals [30,32,37,42]. In particular, in the experiments of Refs. [42] and [30], prepatterned gold targets were bombarded at normal incidence with Ar^+ ions. Although the initial ripples influence the pattern formation substantially—to the extent that dots align preferentially along preexisting ripple ridges leading to so-called nanobead structures, (semi)quantitatively described by the eKS equation—rows of such nanobeads tend to further align in such a way that, on average, each bead has four nearest-neighbor beads: two along the same row and two in the adjacent bead rows. Such short-range ordering had remained beyond description by the eKS model, while it is similar to what is obtained in Fig. 5; compare, e.g., with Fig. 1(c) in Ref. [30].

Systematic numerical integration of the anisotropic model at normal incidence was carried out, which has provided indications on the effect of the various terms in the equation and, consequently, of the underlying mechanisms behind each one. In particular, we have focused on observables such as the roughness W, the wavelengths along the two independent directions, ℓ_x and ℓ_y, and the type of pattern and order that ensues. Two main characteristics should be highlighted: (i) Eq. (8) is able to predict patterns with $\ell_x \neq \ell_y$ and (ii) this continuum model can also predict patterns with short-range square order. Both features have been observed in IBS of metals under normal incidence [30,32,37,42] and had not been predicted by previous models. We have also introduced an angular correlation function which has been proven to usefully characterize quantitatively the pattern symmetry. Furthermore, since the parameters of the equation depend explicitly on physical conditions, it could be possible to design specific experiments to control the resulting pattern if different geometrical properties are required for applications. It is worth mentioning that square patterns have also been observed in IBS experiments on semiconductors (Si and Ge) when metallic contaminants are co-deposited [43,44]. In those cases, the role of metals is twofold: on the one hand they trigger pattern formation even for angles below a critical one (a feature that is not observed on *clean experiments* [48]) and, on the other hand, they introduce anisotropy, as predicted by our model in the present work.

On general grounds, these conclusions seem to substantiate further the applicability of twofield models such as Eqs. (1)–(6) for IBS of metallic systems in the erosive regime. One relevant question in this connection is whether (anisotropy-enhanced) short-range order of the type predicted by this model suffices to account for all of the experimental morphologies, or whether stronger ordering properties are required, akin to those found, e.g., in IBS of binary materials [68].

Finally, the type of model and derivation that we have employed may actually be helpful in two additional contexts in which surface anisotropies play a role. One is IBS of metallic systems under diffusive conditions [32] or of semiconductor targets at high temperatures [33–35]. In both cases the (anisotropic) crystalline structure proves to be of paramount importance. Model (1)–(6) should probably be generalized in order to account for anisotropic surface tension and diffusion, allowing for nonlinear contributions. The second context is that of surface nanopatterning by ion implantation, in which anisotropic surface diffusion terms have been invoked in order to account for experimental patterns with novel symmetries [69].

ACKNOWLEDGMENTS

We acknowledge discussions with J.-S. Kim and J.-H. Kim. This work has been funded through MINECO (Spain) Grants No. FIS2012-38866-C05-01, No. FIS2012-32349, No. FIS2013-47949-C2-2, and No. FIS2015-66020-C2-1-P.

APPENDIX A: PARAMETER VALUES OF THE ANISOTROPIC EFFECTIVE EQUATION

To obtain the effective height equation (7), we follow a multiple-scales approach which is similar to that employed in Refs. [22] and [25], but now assuming anisotropic surface diffusion.

As shown in Sec. II and in Ref. [25],

$$k^{\ell}_{x,y} \sim \epsilon^{1/2}, \quad \mathrm{Re}\,\omega(\boldsymbol{k}^{\ell}) \sim \epsilon^{2}, \quad \mathrm{Im}\,\omega(\boldsymbol{k}^{\ell}) \sim \epsilon^{3/2}, \quad \text{(A1)}$$

where $\boldsymbol{k}^{\ell}$ is the wave vector characterizing the most unstable Fourier mode of the system and $\omega(\boldsymbol{k})$ is the (complex) linear dispersion relation characterizing the dynamics of periodic perturbations around the flat homogeneous solution of the coupled system (1) and (2) [66]. These scalings with ϵ make it natural to consider the spatial variables $X = \epsilon^{1/2}x$ and $Y = \epsilon^{1/2}y$, that are of order unity at scales of the order of the pattern wavelength ℓ, and to define the slow time variables $T_1 = \epsilon^{3/2}t$ and $T_2 = \epsilon^{2}t$, which are associated with the translation and growth of the linear instability, respectively. These variables will allow us to perform a multiple-scale analysis and to obtain an effective (closed) equation for h, instead of a coupled system for R and h. This is possible because the dynamics of R is much faster than that of h.

The derivatives with respect to the original space and time variables are related with the derivatives with respect to the new slow variables by the chain rule, as

$$\frac{\partial}{\partial x} = \epsilon^{1/2}\frac{\partial}{\partial X}, \quad \text{(A2)}$$

$$\frac{\partial}{\partial y} = \epsilon^{1/2}\frac{\partial}{\partial Y}, \quad \text{(A3)}$$

$$\frac{\partial}{\partial t} = \epsilon^{3/2}\frac{\partial}{\partial T_1} + \epsilon^{2}\frac{\partial}{\partial T_2}. \quad \text{(A4)}$$

The coupled equations (1) and (2) can be written in terms of these slow variables as

$$\epsilon^{3/2}\frac{\partial R}{\partial T_1}+\epsilon^2\frac{\partial R}{\partial T_2}=(1-\phi)\Gamma_{\rm ex}-\Gamma_{\rm ad}+\epsilon\nabla\cdot(\boldsymbol{D}\nabla R), \tag{A5}$$

$$\epsilon^{3/2}\frac{\partial h}{\partial T_1}+\epsilon^2\frac{\partial h}{\partial T_2}=-\Gamma_{\rm ex}+\Gamma_{\rm ad}, \tag{A6}$$

where

$$\Gamma_{\rm ad}=\gamma_0\{R-R_{\rm eq}[1-\epsilon\nabla\cdot(\boldsymbol{\Gamma_2}\nabla h)]\}, \tag{A7}$$

$$\Gamma_{\rm ex}=\gamma_0 R_{\rm eq}\left\{\epsilon+\epsilon^{3/2}\alpha_{1x}\frac{\partial h}{\partial X}+\epsilon^2[\nabla\cdot(\boldsymbol{A_2}\nabla h)+\nabla h\cdot(\boldsymbol{A_3}\nabla h)]\right\}, \tag{A8}$$

and

$$\boldsymbol{\Gamma_2}=\mathrm{diag}(\gamma_{2x},\gamma_{2y}),\quad \boldsymbol{A_2}=\mathrm{diag}(\alpha_{2x},\alpha_{2y}),\quad \boldsymbol{A_3}=\mathrm{diag}(\alpha_{3x},\alpha_{3y}),$$

$$\nabla\cdot(\boldsymbol{\Gamma_2}\nabla h)=\gamma_{2x}\frac{\partial^2 h}{\partial X^2}+\gamma_{2y}\frac{\partial^2 h}{\partial Y^2},\quad \nabla\cdot(\boldsymbol{A_2}\nabla h)=\alpha_{2x}\frac{\partial^2 h}{\partial X^2}+\alpha_{2y}\frac{\partial^2 h}{\partial Y^2},\quad \nabla h\cdot(\boldsymbol{A_3}\nabla h)=\alpha_{3x}\left(\frac{\partial h}{\partial X}\right)^2+\alpha_{3y}\left(\frac{\partial h}{\partial Y}\right)^2. \tag{A9}$$

If (A5) and (A6) are added together, we obtain the following equation:

$$\epsilon^{3/2}\frac{\partial h}{\partial T_1}+\epsilon^2\frac{\partial h}{\partial T_2}=-\phi\Gamma_{\rm ex}+\epsilon\nabla\cdot(\boldsymbol{D}\nabla R)-\epsilon^{3/2}\frac{\partial R}{\partial T_1}-\epsilon^2\frac{\partial R}{\partial T_2}. \tag{A10}$$

The method consists of expanding R and h in powers of $\epsilon^{1/2}$ as [25]

$$R=\sum_{n=0}^{\infty}R_n\epsilon^{n/2},\quad h=\sum_{n=0}^{\infty}h_n\epsilon^{n/2}, \tag{A11}$$

and substituting the expansion into Eqs. (A5)–(A8). Equation (A5) is used to obtain the coefficients R_n as functions of lower-order terms in the expansions of R and h. Such values of the coefficients R_n will be substituted into Eq. (A10) and this will allow us to obtain a closed equation for h.

Order ϵ^0. Replacing (A11) in Eq. (A5) and matching the terms at order ϵ^0 on both sides of the equation, we obtain that

$$R_0=R_{\rm eq}. \tag{A12}$$

Order $\epsilon^{1/2}$. At this order, there is no contribution on the right-hand side of Eq. (A5), therefore

$$R_1=0. \tag{A13}$$

Order ϵ^1. Doing the same at this order, we obtain

$$R_2=\bar{\phi}-R_{\rm eq}\nabla\cdot(\boldsymbol{\Gamma_2}\nabla h_0). \tag{A14}$$

Order $\epsilon^{3/2}$. At this order, from Eq. (A5) we obtain

$$R_3=\bar{\phi}\alpha_{1x}\frac{\partial h_0}{\partial X}-R_{\rm eq}\nabla\cdot(\boldsymbol{\Gamma_2}\nabla h_1). \tag{A15}$$

We substitute the values obtained for the expansion of R in Eq. (A10) and we obtain a closed equation for h_0,

$$\frac{\partial h_0}{\partial T_1}=-\bar{\phi}\gamma_0 R_{\rm eq}\alpha_{1x}\frac{\partial h_0}{\partial X}. \tag{A16}$$

Order ϵ^2. From Eq. (A5)

$$R_4=\frac{\bar{\phi}}{\gamma_0}\Gamma_{\rm ex}(\epsilon^2)-R_{\rm eq}\nabla\cdot(\boldsymbol{\Gamma_2}\nabla h_2)+\frac{1}{\gamma_0}\nabla\cdot(\boldsymbol{D}\nabla R_2), \tag{A17}$$

where $\Gamma_{\rm ex}(\epsilon^2)$ denotes the contribution of $\Gamma_{\rm ex}$ at order ϵ^2,

$$\Gamma_{\rm ex}(\epsilon^2)=\gamma_0 R_{\rm eq}\left[\alpha_{1x}\frac{\partial h_1}{\partial X}+\nabla\cdot(\boldsymbol{A_2}\nabla h_0)+\nabla h_0\cdot(\boldsymbol{A_3}\nabla h_0)\right]. \tag{A18}$$

Note that the expansion term R_n to order $\epsilon^{n/2}$ depends only on terms R_m and h_m with $m=0,\ldots,n-2$. To order ϵ^2, Eq. (A10) becomes

$$\frac{\partial h_1}{\partial T_1}+\frac{\partial h_0}{\partial T_2}=\phi\Gamma_{\rm ex}(\epsilon^2)+\nabla\cdot(\boldsymbol{D}\nabla R_2). \tag{A19}$$

Order $\epsilon^{5/2}$. We continue with the procedure and using Eq. (A10) we get

$$\frac{\partial h_2}{\partial T_1}+\frac{\partial h_1}{\partial T_2}=-\phi\Gamma_{\rm ex}(\epsilon^{5/2})+\nabla\cdot(\boldsymbol{D}\nabla R_3)-\frac{\partial R_2}{\partial T_1}, \tag{A20}$$

where $\Gamma_{\rm ex}(\epsilon^{5/2})$ denotes the contribution of order $\epsilon^{5/2}$ to $\Gamma_{\rm ex}$. Using Eqs. (A14) and (A16) we can obtain

$$\frac{\partial R_2}{\partial T_1}=R_{\rm eq}\phi\gamma_0\alpha_{1x}\nabla\cdot\left[\boldsymbol{\Gamma_2}\nabla\left(\frac{\partial h_0}{\partial X}\right)\right]. \tag{A21}$$

Order ϵ^3. At this order, from Eq. (A10) we have

$$\frac{\partial h_3}{\partial T_1}+\frac{\partial h_2}{\partial T_2}=-\phi\Gamma_{\rm ex}(\epsilon^3)+\nabla\cdot(\boldsymbol{D}\nabla R_4)-\frac{\partial R_3}{\partial T_1}-\frac{\partial R_2}{\partial T_2}. \tag{A22}$$

Since $\Gamma_{\rm ex}$ does not depend explicitly on R and we have obtained the R_n terms for $n\leqslant 4$ as functions of h_m with $m\leqslant 2$, we can finally obtain a closed equation for the height h up to order h_3.

The expression which relates the time derivative with the slow time derivatives

$$\frac{\partial}{\partial t}=\epsilon^{3/2}\frac{\partial}{\partial T_1}+\epsilon^2\frac{\partial}{\partial T_2} \tag{A23}$$

allows us to obtain $\partial h/\partial t$ up to order ϵ^3 as

$$\frac{\partial h}{\partial t}=\epsilon^{3/2}\frac{\partial h_0}{\partial T_1}+\epsilon^2\left(\frac{\partial h_0}{\partial T_2}+\frac{\partial h_1}{\partial T_1}\right)+\epsilon^{5/2}\left(\frac{\partial h_1}{\partial T_2}+\frac{\partial h_2}{\partial T_1}\right)+\epsilon^3\left(\frac{\partial h_2}{\partial T_2}+\frac{\partial h_3}{\partial T_1}\right). \tag{A24}$$

In this equation, $\partial_{T_1}h_0$ is given by Eq. (A16) and the terms $(\partial_{T_2}h_n+\partial_{T_1}h_{n+1})$, for $n=0,1,2$, are given by Eqs. (A19), (A20), and (A22), respectively. If we substitute these expressions into Eq. (A24) we obtain

$$\begin{aligned}\frac{\partial h}{\partial t}=&\epsilon^{3/2}\left(-\phi\gamma_0R_{\rm eq}\alpha_{1x}\frac{\partial h}{\partial X}\right)+\epsilon^2\{-\phi\gamma_0R_{\rm eq}[\nabla\cdot(\boldsymbol{A_2}\nabla h)+\nabla h\cdot(\boldsymbol{A_3}\nabla h)]-R_{\rm eq}\nabla\cdot\boldsymbol{D}\nabla[\nabla\cdot(\boldsymbol{\Gamma_2}\nabla h)]\}\\&+\epsilon^{5/2}\left\{\alpha_{1x}\left[\bar\phi\nabla\cdot\boldsymbol{D}\nabla\left(\frac{\partial h}{\partial X}\right)-\phi\gamma_0R_{\rm eq}\nabla\cdot\boldsymbol{\Gamma_2}\nabla\left(\frac{\partial h}{\partial X}\right)\right]\right\}+\epsilon^3\left\{\bar\phi\nabla\cdot\boldsymbol{D}\nabla[\nabla\cdot(\boldsymbol{A_2}\nabla h)+\nabla h\cdot(\boldsymbol{A_3}\nabla h)]\right.\\&\left.-\phi\gamma_0R_{\rm eq}\nabla\cdot(\boldsymbol{\Gamma_2}\nabla[\nabla\cdot(\boldsymbol{A_2}\nabla h)+\nabla h\cdot(\boldsymbol{A_3}\nabla h)])+\bar\phi\phi\gamma_0R_{\rm eq}^2\alpha_{1x}^2\frac{\partial^2h}{\partial X^2}\right\}.\end{aligned} \tag{A25}$$

Equation (A25) is the effective height equation up to order ϵ^3, written in the slow space variables X and Y, in which 6th-order derivatives have been neglected. The final step is to undo the change of variables $X=\epsilon^{1/2}x$ and $Y=\epsilon^{1/2}y$, obtaining

$$\begin{aligned}\frac{\partial h}{\partial t}=&(-\phi\alpha_0\alpha_{1x})\frac{\partial h}{\partial x}+\alpha_{1x}\frac{\alpha_0}{\gamma_0}\left[\bar\phi\nabla\cdot\boldsymbol{D}\nabla\left(\frac{\partial h}{\partial x}\right)-\phi\gamma_0R_{\rm eq}\nabla\cdot\boldsymbol{\Gamma_2}\nabla\left(\frac{\partial h}{\partial x}\right)\right]\\&-\phi\alpha_0[\nabla\cdot(\boldsymbol{A_2}\nabla h)+\nabla h\cdot(\boldsymbol{A_3}\nabla h)]+\frac{\alpha_0^2}{\gamma_0}\bar\phi\phi\alpha_{1x}^2\frac{\partial^2h}{\partial x^2}-R_{\rm eq}\nabla\cdot\boldsymbol{D}\nabla[\nabla\cdot(\boldsymbol{\Gamma_2}\nabla h)]\\&+\frac{\alpha_0}{\gamma_0}\{\bar\phi\nabla\cdot\boldsymbol{D}\nabla[\nabla\cdot(\boldsymbol{A_2}\nabla h)+\nabla h\cdot(\boldsymbol{A_3}\nabla h)]-\phi\gamma_0R_{\rm eq}\nabla\cdot\boldsymbol{\Gamma_2}\nabla[\nabla\cdot(\boldsymbol{A_2}\nabla h)+\nabla h\cdot(\boldsymbol{A_3}\nabla h)]\},\end{aligned} \tag{A26}$$

with

$$\begin{aligned}\nabla\cdot\boldsymbol{D}\nabla[\nabla\cdot(\boldsymbol{\Gamma_2}\nabla h)]&=\sum_{i,j,k=x,y}D_{ij}\gamma_{2k}\frac{\partial^2}{\partial i\partial j}\left(\frac{\partial^2h}{\partial k^2}\right),\quad \nabla\cdot\boldsymbol{D}\nabla[\nabla\cdot(\boldsymbol{A_2}\nabla h)]=\sum_{i,j,k=x,y}D_{ij}\alpha_{2k}\frac{\partial^2}{\partial i\partial j}\left(\frac{\partial^2h}{\partial k^2}\right),\\\nabla\cdot\boldsymbol{\Gamma_2}\nabla[\nabla\cdot(\boldsymbol{A_2}\nabla h)]&=\sum_{i,j,k=x,y}\gamma_{2i}\delta_{ij}\alpha_{2k}\frac{\partial^2}{\partial i\partial j}\left(\frac{\partial^2h}{\partial k^2}\right),\quad \nabla\cdot\boldsymbol{D}\nabla[\nabla h\cdot(\boldsymbol{A_3}\nabla h)]=\sum_{i,j,k=x,y}D_{ij}\alpha_{3k}\frac{\partial^2}{\partial i\partial j}\left(\frac{\partial h}{\partial k}\right)^2,\\\nabla\cdot\boldsymbol{\Gamma_2}\nabla[\nabla h\cdot(\boldsymbol{A_3}\nabla h)]&=\sum_{i,j,k=x,y}\gamma_{2i}\delta_{ij}\alpha_{3k}\frac{\partial^2}{\partial i\partial j}\left(\frac{\partial h}{\partial k}\right)^2,\end{aligned} \tag{A27}$$

where δ_{ij} is the Kronecker delta.

Making use of (A27), we finally obtain a closed expression for h by writing Eq. (A26) as (7), with the coefficients being specifically given by [61]

$$\gamma_x = -\phi\alpha_0\alpha_{1x}, \quad \nu_x = \phi\alpha_0\alpha_{2x} - \frac{\alpha_0^2}{\gamma_0}\bar{\phi}\phi\alpha_{1x}^2, \quad \nu_y = \phi\alpha_0\alpha_{2y}, \quad \Omega_{ij} = \alpha_0\left(\frac{\bar{\phi}D_{ij}}{\gamma_0} - \phi R_{\rm eq}\gamma_{2i}\delta_{ij}\right)\alpha_{1x},$$
$$\mathcal{K}_{ijk} = D_{ij}R_{\rm eq}\gamma_{2k} + \alpha_0\left(\phi R_{\rm eq}\gamma_{2i}\delta_{ij} - \frac{\bar{\phi}D_{ij}}{\gamma_0}\right)\alpha_{2k}, \quad \lambda_i^{(1)} = -\alpha_0\phi\alpha_{3i}, \quad \lambda_{ijk}^{(2)} = \alpha_0\left(\phi R_{\rm eq}\gamma_{2i}\delta_{ij} - \frac{\bar{\phi}D_{ij}}{\gamma_0}\right)\alpha_{3k}, \qquad \text{(A28)}$$

where $i,j,k = x,y$.

[1] T. Som and D. Kanjilal, eds., *Nanofabrication by Ion-beam Sputtering: Fundamentals and Applications* (Pan Stanford Publishing, Singapore, 2013).

[2] F. Buatier de Mongeot and U. Valbusa, Applications of metal surfaces nanostructured by ion beam sputtering, J. Phys.: Condens. Matter **21**, 224022 (2009).

[3] J. Muñoz-García, L. Vázquez, R. Cuerno, J. A. Sánchez-García, M. Castro, and R. Gago, Self-organized surface nanopatterning by ion beam sputtering, in *Toward Functional Nanomaterials*, edited by Z. M. Wang (Springer, New York, 2009), pp. 323–398.

[4] H. Gnaser, *Low Energy Ion Irradiation of Solid Surfaces* (Springer-Verlag, Berlin Heidelberg, 1999).

[5] R. M. Bradley and J. M. E. Harper, Theory of ripple topography induced by ion bombardment, J. Vac. Sci. Technol. A **6**, 2390 (1988).

[6] P. Sigmund, Theory of sputtering. I. Sputtering yield of amorphous and polycrystalline targets, Phys. Rev. **184**, 383 (1969).

[7] W. W. Mullins, Theory of thermal grooving, J. Appl. Phys. **28**, 333 (1957).

[8] R. Cuerno and A.-L. Barabási, Dynamic Scaling of Ion-Sputtered Surfaces, Phys. Rev. Lett. **74**, 4746 (1995).

[9] R. Cuerno, M. Castro, J. Muñoz-García, R. Gago, and L. Vázquez, Nanoscale pattern formation at surfaces under ion-beam sputtering: A perspective from continuum models, Nucl. Instrum. Methods Phys. Res., Sect. B **269**, 894 (2011).

[10] T. Aste and U. Valbusa, Surface instabilities in granular matter and ion-sputtered surfaces, Physica A **332**, 548 (2004).

[11] T. Aste and U. Valbusa, Ripples and ripples: From sandy deserts to ion-sputtered surfaces, New J. Phys. **7**, 122 (2005).

[12] Z. Csahók, C. Misbah, F. Rioual, and A. Valance, Dynamics of aeolian sand ripples, Eur. Phys. J. E **3**, 71 (2000).

[13] T. Tiedje and A. Ballestad, Atomistic basis for continuum growth equation: Description of morphological evolution of GaAs during molecular beam epitaxy, Thin Solid Films **516**, 3705 (2008).

[14] M. Makeev and A.-L. Barabási, Ion-induced effective surface diffusion in ion sputtering, Appl. Phys. Lett. **71**, 2800 (1997).

[15] M. Makeev, R. Cuerno, and A. Barabási, Morphology of ion-sputtered surfaces, Nucl. Instrum. Methods Phys. Res., Sect. B **197**, 185 (2002).

[16] T. C. Kim, C.-M. Ghim, H. J. Kim, D. H. Kim, D. Y. Noh, N. D. Kim, J. W. Chung, J. S. Yang, Y. J. Chang, T. W. Noh *et al.*, Kinetic Roughening of Ion-Sputtered Pd(001) Surface: Beyond the Kuramoto-Sivashinsky Model, Phys. Rev. Lett. **92**, 246104 (2004).

[17] T. C. Kim, C.-M. Ghim, H. J. Kim, D. H. Kim, D. Y. Noh, N. D. Kim, J. W. Chung, J. S. Yang, Y. J. Chang, T. W. Noh *et al.*, Reply to Comment on Kinetic Roughening of Ion-Sputtered Pd(001) Surface: Beyond the Kuramoto-Sivashinsky Model, Phys. Rev. Lett. **94**, 139602 (2005).

[18] M. Castro and R. Cuerno, Comment on Kinetic Roughening of Ion-Sputtered Pd(001) Surface: Beyond the Kuramoto-Sivashinsky Model, Phys. Rev. Lett. **94**, 139601 (2005).

[19] S. More and R. Kree, Non-local linear stability of ion beam eroded surfaces, Appl. Surf. Sci. **258**, 4179 (2012).

[20] R. M. Bradley, Exact linear dispersion relation for the Sigmund model of ion sputtering, Phys. Rev. B **84**, 075413 (2011).

[21] M. Castro, R. Cuerno, L. Vázquez, and R. Gago, Self-Organized Ordering of Nanostructures Produced by Ion-Beam Sputtering, Phys. Rev. Lett. **94**, 016102 (2005).

[22] J. Muñoz-García, M. Castro, and R. Cuerno, Nonlinear Ripple Dynamics on Amorphous Surfaces Patterned by Ion Beam Sputtering, Phys. Rev. Lett. **96**, 086101 (2006).

[23] J. Muñoz-García, R. Cuerno, and M. Castro, Short-range stationary patterns and long-range disorder in an evolution equation for one-dimensional interfaces, Phys. Rev. E **74**, 050103(R) (2006).

[24] J. Muñoz-García, R. Cuerno, and M. Castro, Coupling of morphology to surface transport in ion-beam-irradiated surfaces: Normal incidence and rotating targets, J. Phys.: Condens. Matter **21**, 224020 (2009).

[25] J. Muñoz-García, R. Cuerno, and M. Castro, Coupling of morphology to surface transport in ion-beam irradiated surfaces: Oblique incidence, Phys. Rev. B **78**, 205408 (2008).

[26] M. Castro and R. Cuerno, Hydrodynamic approach to surface pattern formation by ion beams, Appl. Surf. Sci. **258**, 4171 (2012).

[27] R. Gago, L. Vázquez, O. Plantevin, J. A. Sánchez-García, M. Varela, M. C. Ballesteros, J. M. Albella, and T. H. Metzger, Temperature influence on the production of nanodot patterns by ion beam sputtering of Si(001), Phys. Rev. B **73**, 155414 (2006).

[28] J. Muñoz-García, R. Gago, L. Vázquez, J. A. Sánchez-García, and R. Cuerno, Observation and Modeling of Interrupted Pattern Coarsening: Surface Nanostructuring by Ion Erosion, Phys. Rev. Lett. **104**, 026101 (2010).

[29] O. Bikondoa, D. Carbone, V. Chamard, and T. H. Metzger, Ion beam sputtered surface dynamics investigated with two-time correlation functions: A model study, J. Phys.: Condens. Matter **24**, 445006 (2012).

[30] J.-H. Kim, J.-S. Kim, J. Muñoz-García, and R. Cuerno, Role of nonlinearities and initial prepatterned surfaces in nanobead

formation by ion-beam bombardment of Au (001): Experiments and theory, Phys. Rev. B **87**, 085438 (2013).
[31] D. Kramczynski, B. Reuscher, and H. Gnaser, Wavelength-dependent ripple propagation on ion-irradiated prepatterned surfaces driven by viscous flow corroborates two-field continuum model, Phys. Rev. B **89**, 205422 (2014).
[32] U. Valbusa, C. Boragno, and F. Buatier de Mongeot, Nanostructuring surfaces by ion sputtering, J. Phys.: Condens. Matter **14**, 8153 (2002).
[33] X. Ou, A. Keller, M. Helm, J. Fassbender, and S. Facsko, Reverse Epitaxy of Ge: Ordered and Faceted Surface Patterns, Phys. Rev. Lett. **111**, 016101 (2013).
[34] X. Ou and S. Facsko, Crystalline nanostructures on Ge surfaces induced by ion irradiation, Nucl. Instrum. Methods Phys. Res., Sect. B **341**, 13 (2014).
[35] X. Ou and S. Facsko, Faceted nanostructure arrays with extreme regularity by self-assembly of vacancies, Nanoscale **7**, 18928 (2015).
[36] W. L. Chan and E. Chason, Making waves: Kinetic processes controlling surface evolution during low energy ion sputtering, J. Appl. Phys. **101**, 121301 (2007).
[37] S. Rusponi, G. Costantini, C. Boragno, and U. Valbusa, Ripple Wave Vector Rotation in Anisotropic Crystal Sputtering, Phys. Rev. Lett. **81**, 2735 (1998).
[38] G. Costantini, S. Rusponi, F. B. de Mongeot, C. Boragno, and U. Valbusa, Periodic structures induced by normal-incidence sputtering on Ag(110) and Ag(001): Flux and temperature dependence, J. Phys.: Condens. Matter **13**, 5875 (2001).
[39] L. Golubović, A. Levandovsky, and D. Moldovan, Epitaxial Growth and Erosion on (110) Crystal Surfaces: Structure and Dynamics of Interfacial States, Phys. Rev. Lett. **89**, 266104 (2002).
[40] A. Levandovsky, L. Golubović, and D. Moldovan, Interfacial states and far-from-equilibrium transitions in the epitaxial growth and erosion on (110) crystal surfaces, Phys. Rev. E **74**, 061601 (2006).
[41] C. Misbah, O. Pierre-Louis, and Y. Saito, Crystal surfaces in and out of equilibrium: A modern view, Rev. Mod. Phys. **82**, 981 (2010).
[42] J. Kim, N. Ha, J. Kim, M. Joe, K. Lee, and R. Cuerno, One-dimensional pattern of Au nanodots by ion-beam sputtering: Formation and mechanism, Nanotechnology **22**, 285301 (2011).
[43] F. Frost, B. Ziberi, T. Höche, and B. Rauschenbach, The shape and ordering of self-organized nanostructures by ion sputtering, Nucl. Instrum. Methods Phys. Res., Sect. B **216**, 9 (2004).
[44] F. Frost, B. Ziberi, A. Schindler, and B. Rauschenbach, Surface engineering with ion beams: From self-organized nanostructures to ultra-smooth surfaces, Appl. Phys. A **91**, 551 (2008).
[45] S. A. Norris, Stress-induced patterns in ion-irradiated silicon: Model based on anisotropic plastic flow, Phys. Rev. B **86**, 235405 (2012).
[46] M. Castro, R. Gago, L. Vázquez, J. Muñoz-García, and R. Cuerno, Stress-induced solid flow drives surface nanopatterning of silicon by ion-beam irradiation, Phys. Rev. B **86**, 214107 (2012).
[47] G. Carter and V. Vishnyakov, Roughening and ripple instabilities on ion-bombarded Si, Phys. Rev. B **54**, 17647 (1996).
[48] J. Muñoz-García, L. Vázquez, M. Castro, R. Gago, A. Redondo-Cubero, A. Moreno-Barrado, and R. Cuerno, Self-organized nanopatterning of silicon surfaces by ion beam sputtering, Mater. Sci. Eng., R **86**, 1 (2014).
[49] R. M. Bradley and P. D. Shipman, A surface layer of altered composition can play a key role in nanoscale pattern formation induced by ion bombardment, Appl. Surf. Sci. **258**, 4161 (2012).
[50] C. C. Umbach, R. L. Headrick, and K.-C. Chang, Spontaneous Nanoscale Corrugation of Ion-Eroded SiO_2: The Role of Ion-Irradiation-Enhanced Viscous Flow, Phys. Rev. Lett. **87**, 246104 (2001).
[51] T. Ala-Nissila, R. Ferrando, and S. C. Ying, Collective and single particle diffusion on surfaces, Adv. Phys. **51**, 949 (2002).
[52] S. H. Davis, *Theory of Solidification* (Cambridge University Press, Cambridge, 2001).
[53] Y. Mo, J. Kleiner, M. Webb, and M. Lagally, Activation Energy for Surface Diffusion of Si on Si (001): A Scanning-Tunneling-Microscopy Study, Phys. Rev. Lett. **66**, 1998 (1991).
[54] R. Ferrando and G. Tréglia, Anisotropy of diffusion along steps on the (111) faces of gold and silver, Phys. Rev. B **50**, 12104 (1994).
[55] G. Danker, O. Pierre-Louis, K. Kassner, and C. Misbah, Peculiar Effects of Anisotropic Diffusion on Dynamics of Vicinal Surfaces, Phys. Rev. Lett. **93**, 185504 (2004).
[56] E. Meca, V. B. Shenoy, and J. Lowengrub, Phase-field modeling of two-dimensional crystal growth with anisotropic diffusion, Phys. Rev. E **88**, 052409 (2013).
[57] E. Meca, J. Lowengrub, H. Kim, C. Mattevi, and V. B. Shenoy, Epitaxial graphene growth and shape dynamics on copper: Phase-field modeling and experiments, Nano Lett. **13**, 5692 (2013).
[58] T. Michely and J. Krug, *Islands, Mounds and Atoms* (Springer Science & Business Media, Berlin Heidelberg, 2004).
[59] S. A. Norris, J. Samela, L. Bukonte, M. Backman, F. Djurabekova, K. Nordlund, C. S. Madi, M. P. Brenner, and M. J. Aziz, Molecular dynamics of single-particle impacts predicts phase diagrams for large scale pattern formation, Nat. Commun. **2**, 276 (2011).
[60] M. P. Harrison and R. M. Bradley, Crater function approach to ion-induced nanoscale pattern formation: Craters for flat surfaces are insufficient, Phys. Rev. B **89**, 245401 (2014).
[61] J. Renedo, Modeling and numerical simulation of ion-beam irradiated surfaces with anisotropic diffusion, Masters thesis, Universidad Carlos III de Madrid, 2013.
[62] M. Rost and J. Krug, Anisotropic Kuramoto-Sivashinsky Equation for Surface Growth and Erosion, Phys. Rev. Lett. **75**, 3894 (1995).
[63] J. Muñoz-García, R. Gago, R. Cuerno, J. Sánchez-García, A. Redondo-Cubero, M. Castro, and L. Vázquez, Independence of interrupted coarsening on initial system order: Ion-beam nanopatterning of amorphous versus crystalline silicon targets, J. Phys.: Condens. Matter **24**, 375302 (2012).
[64] C.-H. Lam and F. G. Shin, Improved discretization of the Kardar-Parisi-Zhang equation, Phys. Rev. E **58**, 5592 (1998).
[65] Y.-P. Zhao, G.-C. Wang, and T.-M. Lu, *Characterization of Amorphous and Crystalline Rough Surfaces: Principles and Applications* (Academic Press, San Diego, 2001).
[66] M. Cross and H. Greenside, *Pattern Formation and Dynamics in Nonequilibrium Systems* (Cambridge University Press, Cambridge, 2009).

[67] C. Gollwitzer, I. Rehberg, and R. Richter, Via hexagons to squares in ferrofluids: Experiments on hysteretic surface transformations under variation of the normal magnetic field, J. Phys.: Condens. Matter **18**, S2643 (2006).

[68] D. A. Pearson, R. M. Bradley, F. C. Motta, and P. D. Shipman, Producing nanodot arrays with improved hexagonal order by patterning surfaces before ion sputtering, Phys. Rev. E **92**, 062401 (2015).

[69] S. A. Mollick, D. Ghose, P. D. Shipman, and R. M. Bradley, Anomalous patterns and nearly defect-free ripples produced by bombarding silicon and germanium with a beam of gold ions, Appl. Phys. Lett. **104**, 043103 (2014).